

A Consistent Averaging Procedure for Solving the Navier Stokes Equations Numerically with Applications to Hypersonic Flow Devices

J. Mendez*, M. Atkinson*, M. Dhanasar*, F. Ferguson*
Corresponding author: fferguso@ncat.edu

* North Carolina A&T State University, Greensboro, NC, USA.

Abstract: High-fidelity hypersonic computations have become practical in recent years. Large Eddy Simulations (LES) and high order shock-capturing schemes, such as ENO and WENO, are able to compute high-speed, three-dimensional flow. However, common application of such schemes is limited by high computational costs and uncertainty errors that are difficult to quantify. A novel technique called *Integro-Differential Scheme* (IDS) may have the capability to alleviate these current limitations. Unlike common numerical techniques where the solution is integrated in time using local information, this method reconstructs the temporal and spatial fluxes using a consistent averaging procedure. This paper focuses on the accuracy with which the IDS predicts the complex physics involved in hypersonic flow devices such as isolators and flame holders. Accurate numerical prediction of such devices is critical in the design and development of supersonic combustion air-breathing engines, also known as Scramjets. The goal of the study is to demonstrate the validity of the IDS by computing supersonic flow in an isolator and flame holding cavity for comparison to experimental data.

Keywords: Numerical Scheme, Hypersonic Flows, CFD, Shock Capturing.

1 Introduction

The closed system of five equations relative to five unknowns described by the *Navier-Stokes Equations* (NSE) can solve a wide range of problems regardless of the boundary and initial conditions. However, the wide range of spatial and temporal scales involved in engineering flows make the task of obtaining an approximate solution difficult. In fact, *Direct Numerical Simulations* (DNS) solves all the scales explicitly, but the computational cost associated with DNS is prohibitively expensive. Consequently, other numerical techniques have emerged such as *Reynolds Averaged Navier Stokes Equations* (RANS) and LES. The former is built upon a low-order statistical approach, whereas the latter resolves the large anisotropic scales while modeling only the homogeneous small ones. Although they provide high quality approximate solutions, the data set representing the numerical solution does not calculate all of the flow characteristics and rely on numerical modeling to predict unresolved flow structures. This leads to challenges when determining properties such as flow separation and transition. In addition, at high speed the flow becomes compressible and contain flow discontinuities (shockwaves); many CFD schemes are unstable or deliver unphysical results under the presence of such discontinuities. For example, eddy viscosity models are widely used in RANS, and under the presence of shocks the production of turbulent kinetic energy is proportional to S_{ii}^2 which is very large in magnitude. In contrast, LES implementations typically require high order schemes and therefore the solution diverges when those discontinuities are present. To maintain the computational stability, artificial dissipation is added under the presence of shocks. As a result, any technique employed to solve these equations must be adapted, modified, or simplified to solve different flow types. These simplifications introduce errors influencing the approximate solution delivered by CFD schemes. In an effort to reduce these errors, Elamin [1] introduced the IDS. This scheme combines the finite volume and finite difference methods. The IDS uses the mean value theorem to construct the fluxes, transforming the integral equations into their finite difference

counterpart. Since the method uses the integral representation of the governing laws, the IDS enforces conservation. The strength of the IDS rests on the numerical approach used to solve the NSE. The scheme is based on an explicit time marching and it applies a consistent averaging procedure in the computation of viscous, inviscid and temporal fluxes. More important, it solves the NSE without numerical models. The latter characteristic highlights the advantages of the IDS since there is no uncertainty connected to semi-empirical models.

The purpose of this study is to demonstrate the physics capturing capabilities of the IDS to resolve highly compressible flow. More specifically, it concentrates on the numerical analysis of Supersonic Combustion Ramjets (Scramjets), where the Isolator and the flame holder section are thoroughly analyzed, refer to Figure 1. The motivation of this analysis is the need to achieve efficient hypersonic combustion. However, the flow physics of the isolator is very challenging due to: shock-wave/boundary-layer interaction, shock-turbulence interaction, and shock-shock interactions. Similarly, the flame holder is composed of a cavity that can produce complex unsteady flowfields causing practical concern in aerospace applications. In addition, other complications pertaining to ignition of the fuel are still active areas of research (e.g. nozzle orientation, mixing efficiency between fuel and air and shape of cavity). Cai *et al.* [2] performed a numerical study to analyze the effect of the cavity geometry and the method of fuel injection. They found that a rearwall-expansion cavity had better performance characteristics compared to other geometries, and the injection method and position affect the stabilization of the flame. In a similar work, Mahto *et al.* [3] studied the effect of variation of length-to-depth ratio and Mach number of a double cavity Scramjet combustor. They demonstrated that there is an optimal cavity length-to-depth ratio for which the performance of combustor significantly improves. However, most of these studies do not consider the full Scramjet configuration, interested readers should refer to [4–7]. Instead they impose a uniform inlet boundary condition, and thus, the strong oblique shock emanating from the Forebody ramp is neglected. Currently, among the new conceptions to improve the understanding of such complex flow configurations, there is a new technique called *zonal method*. This approach applies different numerical simulations for the different parts of the Scramjet. For example, the first simulation aims at evaluating the flow physics from the Forebody ramp discharging into the Isolator. These results are then used as an inlet boundary condition for the combustion section. This approach has shown to be very effective for evaluating the HyShot II Scramjet [8–10]. This study implements the zonal method to study a Generic Hypersonic Vehicle (GHV) [11] using the IDS where the design of the ideal Scramjet is based on the performance of the Isolator. Thus, this study is an inversed engineering approach. In other words, we select the right geometric parameters based on the Isolator performance. Unlike the HyShot II, the GHV does not have a shock-trap and therefore shocks from the upper and lower lip entering the Isolator are strong.

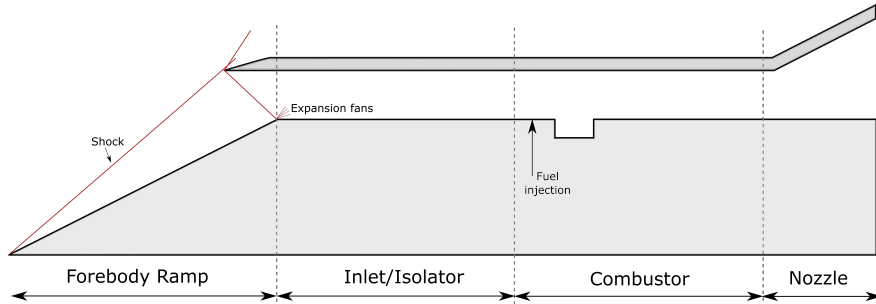


Figure 1: Schematic diagram of the GHV.

This study uses an engineering model presented by Matsuo *et al.* [12] to predict the length of pseudo-shock on the Isolator. To this end, a supersonic inlet diffuser domain was created in cartesian coordinates and the inlet boundary conditions are extracted from the $\theta - \beta - Ma$ relation [13]. The sketch of the computational domain is shown in Figure 2 along with the freestream conditions. In addition, Figure 2 depicts important flow features that are expected to be recovered in the numerical computation, such as a strong oblique shock emanating from the leading edge and reflected shocks. The secondary objective of this analysis is to evaluate the influence of the geometric parameters on the overall performance of the Isolator. The varying parameters are the height of the isolator (D) and the effective length of the isolator ($L_p - L_i$). The efficiency of the

isolator is measured in terms of the static pressure recovery. Once the most effective geometric configuration is obtained, the solution is coupled with the flame holder device, the cavity. The primary objective of this numerical study is to explore the complex flow physics of the Isolator and cavity using the IDS.

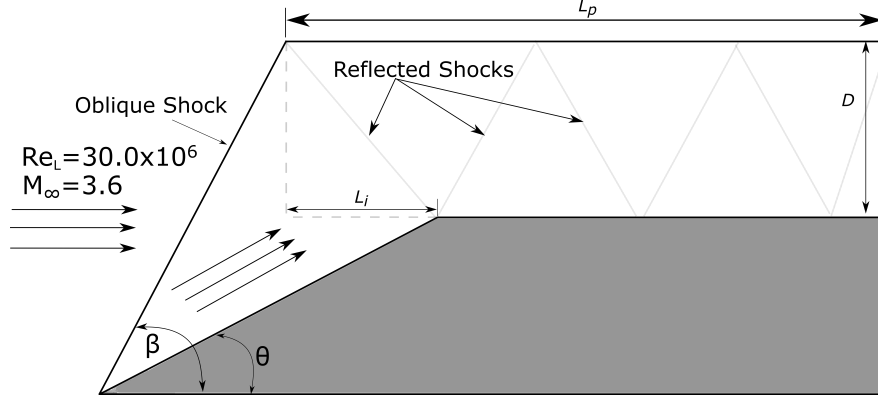


Figure 2: IDS domain mapping for the pseudo shock problem.

2 Governing Equations and Numerical Method

2.1 The Navier Stokes Equations

Numerical solutions of fluid dynamic problems are governed by conservation laws. These laws can be expressed mathematically either in the differential or the integral form. In the case of compressible fluid flows, these coupled laws form a closed system of partial differential equations. Herein, the conservation of mass, momentum and energy in the integral form are of interest to this study, and they are expressed as follows:

$$\frac{\partial}{\partial t} \iiint_V \rho dv + \iint_S ((\rho u)_i \cdot dS_i) = 0 \quad (1)$$

$$\frac{\partial}{\partial t} \iiint_V (\rho u)_k dv + \iint_S ((\rho u)_i \cdot dS_i) u_k = - \iint_S (P dS_k) + \iint_S \hat{\tau}_{ik} \cdot dS_i \quad (2)$$

$$\frac{\partial}{\partial t} \iiint_V (\rho E) dv + \iint_S ((\rho E u)_i \cdot dS_i) = - \iint_S (P u_i \cdot dS_i) + \iint_S ((\hat{\tau}_{ik} u_k) \cdot dS_i) + \iint_S (q_i dS_i) \quad (3)$$

In equation (1 - 3) the symbols: ρ , u , t represent the density, the velocity components of an elementary control fluid element, and time, respectively. In addition, the symbols E , P , τ_{ik} and q_i in equations (1 - 3) represent the internal energy, pressure, the stress tensor and the heat flux associated with an elementary control volume, respectively. Internal energy, pressure, stress tensor and heat flux are defined by equations (4 - 7),

$$E = C_v T + \frac{1}{2} u_k u_k \quad (4)$$

$$P = \rho R T \quad (5)$$

$$\tau_{ik} = \mu \left(\frac{\partial u_i}{\partial x_k} + \frac{\partial u_k}{\partial x_i} - \frac{2}{3} \delta_{ik} \frac{\partial u_j}{\partial x_k} \right) \quad (6)$$

$$q_k = -K \frac{\partial T}{\partial x_k} \quad (7)$$

In equation (5), R is the gas constant. The symbols μ and k represent the viscous and thermal properties of the fluid of interest. For air, the viscosity of the fluid is evaluated using Sutherland's law,

$$\mu = \mu_\infty \left(\frac{T}{T_\infty} \right)^{3/2} \frac{T_\infty + 110}{T + 110} \quad (8)$$

and the thermal conductivity expression,

$$k = f(T) \quad (9)$$

is provided. In the case of 3D aerothermodynamics, the NSE (1 - 9) represent a closed system of five equations relative to 5 unknowns. These unknowns are called Primitive Variables (PV), and are defined in the vector form as follows:

$$PV := [\rho \ u \ v \ w \ T]^T \quad (10)$$

Equations (1-9) generate a unique solution set, only when the appropriate set of initial and boundary conditions are provided.

2.2 Overview of the *Integro-Differential Scheme (IDS)*

The primitive variables associated with equations (1-9) are evaluated using the IDS procedure, which was described in Ferguson *et al.* [14], and the details are not repeated herein. In a more recent study, Ferguson *et al.* [15] demonstrated that the order of accuracy of the IDS is second order for fine meshes while it remains between first and second order for coarser meshes. However, the purpose of this section is to showcase the main differences between the conventional Finite Volume Method (FVM) and the Finite Difference Method (FDM). The IDS formulation uses the integral form of the NSE, and thus, it enforces conservation of the discrete quantities, namely, mass, momentum, and energy. This fact highlights the good physical and mathematical characteristics of the scheme since the correct wave velocity propagation is ensured [16]. In the developmental stages of this research and for illustration purposes, a typical flow field is represented by a rectangular domain and a typical elementary fluid element represented by a rectangular prism, refer to Figure 3. Figure 3 represents the Integro-Differential Model (IDM) as it is applied to the computational solution to the NSE (1-8). In general, the IDS solution of a given fluid dynamic problem is built on an interconnecting set of *spatial* and *temporal* cells. In the Cartesian system of coordinates, a typical fluid cell is nothing more than a carefully chosen elementary rectangular prism, defined by the dimension; dx , dy and dz . It is the application of a specified fluid cell in relationship to the NSE equations that determines whether it becomes a spatial cell or a temporal control volume.

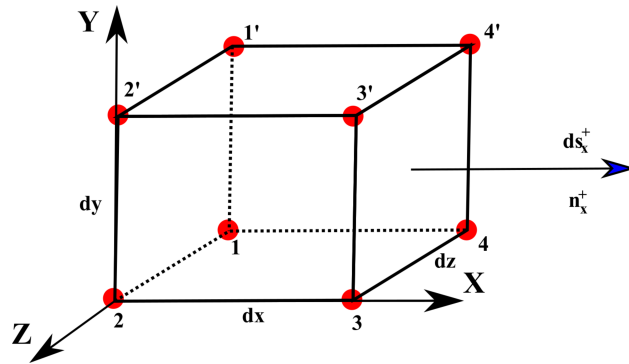


Figure 3: Spatial cell with notation at surfaces nodes

A given cell is defined locally by six independent surfaces, and each surface defined by four nodes, with the set of four nodes lying in a given plane. Additionally, plus and minus notations define the unit normal, n , with respect to each surface. Next, each surface of each cell is defined by four nodes. Each term in the NSE (1-3) are applied systematically to each cell, and thus they are called *spatial* cells. The mean value theorem is invoked and a set of algebraic equations representing the rate of change of mass, momentum,

and energy associated with each spatial cell is derived. However, the rates of change of the time-fluxes are not associated with any grid point, but with the spatial cell. Analogous to the spatial cells, the concept of a *temporal* cell is also introduced. The *temporal* cells are defined as rectangular prisms formed from the center points of the eight neighboring *spatial* cells. Finally, the concept of a computational control volume is defined, as a collection of eight *spatial* cells and one integrated *temporal* cell. An IDS representation of the computational control volume is illustrated in Figure 4.

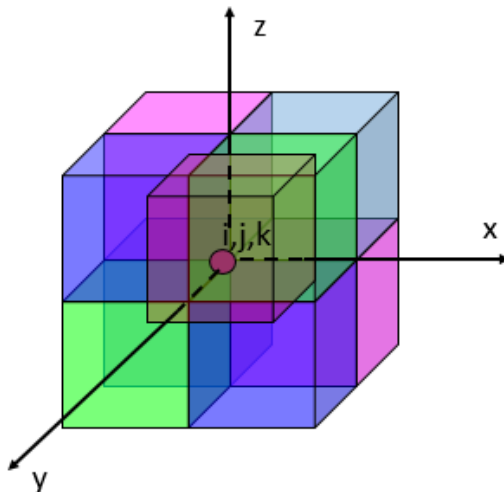


Figure 4: IDS computational control volume

It is of interest to note that inviscid fluxes are computed with the local information of the *spatial* cells. However, two additional and adjacent surfaces in each directions are needed for evaluating the viscous terms. Finally, the time marching technique is based on the Taylor's expansions series and it is shown in equation (11). This implementation involves a unique technique to compute the right hand side terms from equations (11) where a averaging procedure is used to compute the solution vector and the time derivative, interested readers refer to [14].

$$(PV)_{i,j}^{t+\Delta t} = (PV)_{i,j}^t + \left(\frac{dPV}{dt} \right)_{ij} \Delta t \quad (11)$$

3 CFD Evaluation of GHV Using the IDS

3.1 Physical Model

The propulsion system of hypersonic vehicles use a combination of wedge angles in the external section to create a family of compression waves. The static pressure increases through the compression waves whereas the total pressure decreases. Although the forebody provides a strong primary shock, secondary weak reflected shocks take place in the *Isolator* converting the kinetic energy into potential energy while maintaining a stable supersonic airflow for the combustion process. Theoretically, there are many reflected shocks, and as a group, they form the shock train within the *Isolator* [11]. These reflections interact with the boundary layer yielding to regions with large adverse pressure gradients and flow separation. In addition, the combustion process produces instabilities changing the back pressure in the *Isolator*. In some cases the pressure can reach very large values, forcing the shock waves to be pushed out of the *Isolator* and inlet, causing a condition called *inlet unstart* [17]. Besides of providing a homogeneous flow to the combustor, the *Isolator isolates* the inlet from the disturbances that may arise from the high pressure because of the intense turbulent combustion [18]. Because of this, the aerodynamic design of hypersonic inlets, as well as *Isolators*, is critical in hypersonic vehicles.

The main objective of this section is to define the height and length of the Isolator with minimal total pressure loss and maximum static pressure recovery for the conditions shown in Figure 2. In this developmental stage, the forebody is represented by one wedge and the area of the scramjet Isolator remains constant. In other words, no divergent angle is used, although Huang *et al.* [19] demonstrated that small divergent angles can influence shock wave transition in the Isolator. The length of the Isolator remains constant for the different test cases, since an excessively long Isolator might lead to an increase in viscous losses thus reducing the maximum pressure recovery. Reinartz *et al.* [20] showed that the length of the Isolator influenced the ability of Isolator to protect the inlet against pressure disturbances. However, a further extension of the duct seemed to have no additional improvement. Therefore, the geometric parameter studied in this section is the height of the Isolator. In contrast to Wang *et al.* [18], where the Waltrup and Billig correlations were used, this section follows the process presented by Matsuo *et al.* [12]. From an engineering perspective, it might be practical to obtain the necessary length to maximize the pressure recovery for such flows. For this type of flow configuration, the length must be at least greater than the "pseudo-shock" length. The "Pseudo shock" is defined as the distance from the onset of pressure rise to the point where pressure achieves its maximum value [12].

Figure 5 depicts the relationship between the length of the pseudo-shock (L_p) divided by the height of the Isolator (D) with the Mach number upstream of the shock M_{1e} . The diamonds, circles, black and white squares represent experimental data, interested readers refer to [12]. It is clearly shown in Figure 5 the scattering in the experimental data. Nevertheless, the experimental data shows a clear tendency similar to the Diffusion model shown in [12], represented by a solid line in the center of the full envelope. Finally, Figure 5 demonstrates that the length of the pseudo-shock increases as the Mach number upstream of the shock increases. For example, for the freestream Mach number used in this study $M_\infty = 3.6$ the Mach number found behind the strong primary shock and a weaker reflected shock is around 2.49, based on the $\theta - \beta - Ma$ relation [13]. Under these conditions, the length of the pseudo-shock can be in between 8-15 times the diameter of the Isolator.

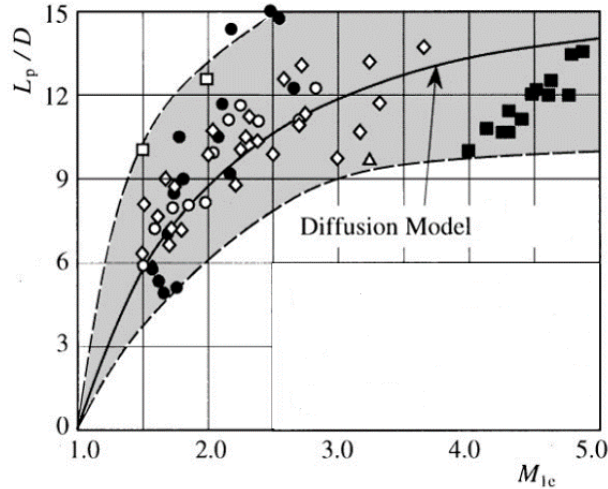


Figure 5: Non-dimensional pseudo-shock length in a constant area duct versus Mach number [12]

We follow an inverse procedure, the diameter of the Isolator is obtained from Figure 5 and three different geometric configurations are chosen. Table 1 shows the three different cases used. Each case has a different value of L_p/D , for example $L_p/D = 16.69$ is chosen for Case 1, whereas $L_p/D = 12.0$ and $L_p/D = 6.0$, for Case 2 and Case 3, respectively. The dimension L_i was chosen such that the angle of the weak reflected shock remained constant for the three different cases.

Table 1: Geometric configurations with a wedge angle $\theta = 10^\circ$

Cases	L_p/D	D	L_i
Case 1	16.69	0.0599	0.1898
Case 2	12	0.080	0.25
Case 3	6	0.166	0.526

3.2 Numerical Solution of the Scramjet Isolator

The IDS formulation is used to compute the flow field in the Scramjet Isolator. The air is considered to be calorically perfect with constant ratio of specific heat as $\gamma = 1.4$. Consider the case of a hypersonic flow where the Mach number entering the Isolator $M_\infty = 3.6$. Under these conditions, the Reynolds number based on the length of the Isolator is $Re_L = 30 \times 10^6$. The length of the Isolator was fixed at 1.0 m, and a Prandtl number of 0.711. The freestream density, temperature, viscosity, and pressure were assumed to be 0.435 kg/m^3 , 281.159 K, $1.7554 \times 10^{-5} \text{ kg/m} \cdot \text{s}$, and 35 KPa, respectively. Pressure is obtained from the equation of state, thus ideal gas approximation is enforced.

The final numerical solution is obtained in two steps. Firstly, the Isolator region (Domain I) is solved using the boundary conditions shown in Figure 6. An adiabatic no-slip boundary condition was enforced at the solid walls on both domains. The solid walls are represented by solid black lines. The supersonic outflow is enforced by extrapolating the primitive variables to the outlet plane from the interior nodes using a second order extrapolation technique. The solution is marched in time from the initial conditions, where the primitive variables are set to their freestream values, until the largest $L^2 - Norm$ of the residuals is below 1.0×10^{-5} . Once the Domain I has reached the steady state solution, the primitive variables are extracted in the plane $Imax - 1$, where $Imax$ represents the maximum numbers of nodes in the horizontal direction. This plane is represented by a red line in Figure 6. It contains the discrete values for the primitive variables from $j = 1, Jmax$, where j represent the indices in the vertical direction. These values are used as inflow conditions for the Domain II. It is important to mention that Domain II was also solved using supersonic inlet boundary conditions rather than using the zonal method described earlier, this case is termed as "*Clean flow*". The objective of this test is to showcase the importance of including the Isolator/Inlet when investigating cavity flameholder.

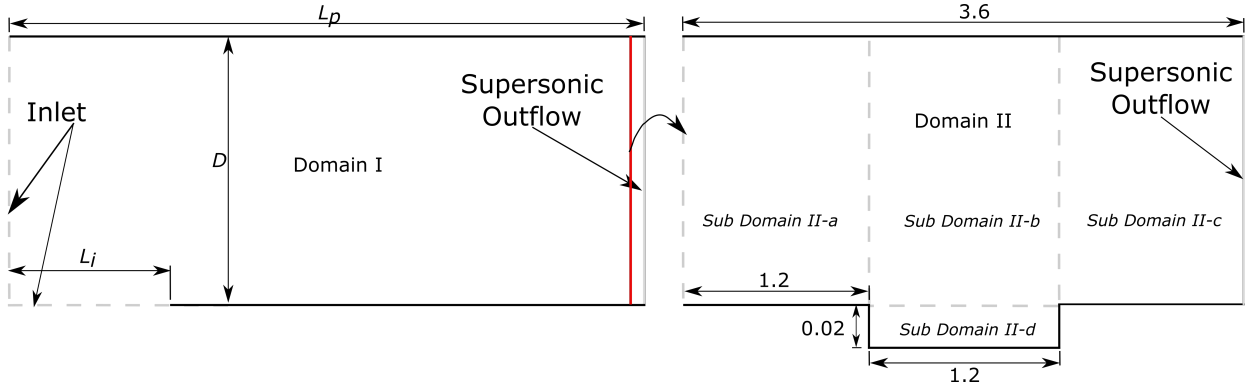


Figure 6: Computational domain and boundary conditions.

A grid study was completed to verify that the numerical solution obtained is grid independent. For this analysis Case 2 was chosen. However, since no turbulence model or wall model were implemented in this study, the grid independent solution will tend towards a Direct Numerical Simulation (DNS) type solution. Thus, slight differences will be found between mesh resolutions used in this study. The goal is to obtain a difference between two consecutive meshes less than 5 %. Figure 7 shows the wall pressure for the three different meshes. The difference in pressure between the fine and medium meshes was 4.7%, whereas the difference found between the coarse and medium meshes was 5.10% and 10 % between the finest and the

Table 2: Grid Characteristics

Mesh	Averaged Pressure
Fine (4001x4001)	5.244
Medium (2001x2001)	5.513
Coarse (1001x1001)	5.229

coarsest meshes.

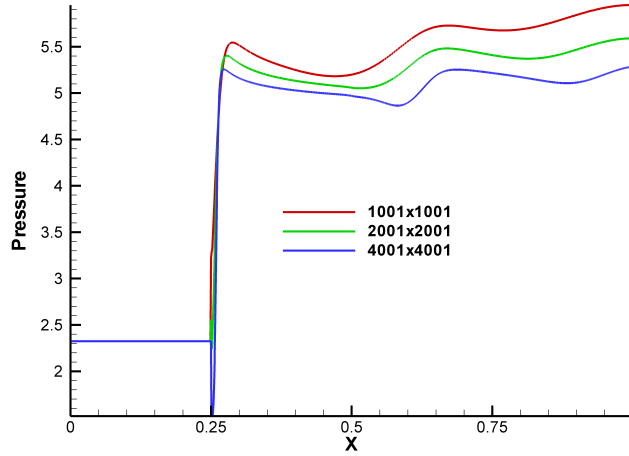


Figure 7: Wall pressure for three different meshes.

Although the percentile difference is below the threshold defined before, it is worth mentioning that the difference in terms of the boundary layer height between the different meshes was considerably high; 22% for the smallest difference. Therefore, a quantitative measure of the grid resolution was performed. To this end, we followed the approach presented in [21] and the pressure recovery at the outlet of the Isolator was chosen to perform such study. Table 2 presents the averaged pressure at the outlet plane for the three different used meshes. The pressure recovery at zero grid spacing was estimated using Richardson extrapolation, and the estimated value was 4.7787. On the other hand, the smaller Grid Convergence Index (GCI) was 10.77%, whereas the maximum GCI found was 16.66%. The latter corresponds to the coarse and medium meshes, while the former represents the GCI for the fine and medium meshes. Also, the asymptotic range of convergence obtained for this data set was 0.94. Thus, the solution is not technically in the asymptotic range of convergence. Based on the previous information, we conclude that the solution is not grid independent and the results presented herein can be considered only as preliminary results. However, the variables of interests for this study (static and total pressure) did not show large differences and the resolution used (4001x4001) is sufficient to capture the physically relevant features.

Figure 8 (a-d) depicts the contour plots for the primitive variables representing Case 2. Figure 8a represents the contour plot for the streamwise velocity component (U) and it shows a thin boundary layer. Also, it is clearly shown that the boundary layer height increases as the flow develops and interacts with the shock waves. This effect is expected because the boundary layer thickens under the presence of adverse pressure gradients, causing an increase in the shape factor and pushing the external flow away from the wall. This effect is also demonstrated in Figure 8(b) where the vertical component of the velocity vector switches signs, thus direction, after the shock interacts with the boundary layer. Furthermore, Figures 8(c) and 8(d) show the density and temperature contour plots. Both plots show an increase density and temperature due

to the presence of weak reflected shocks.

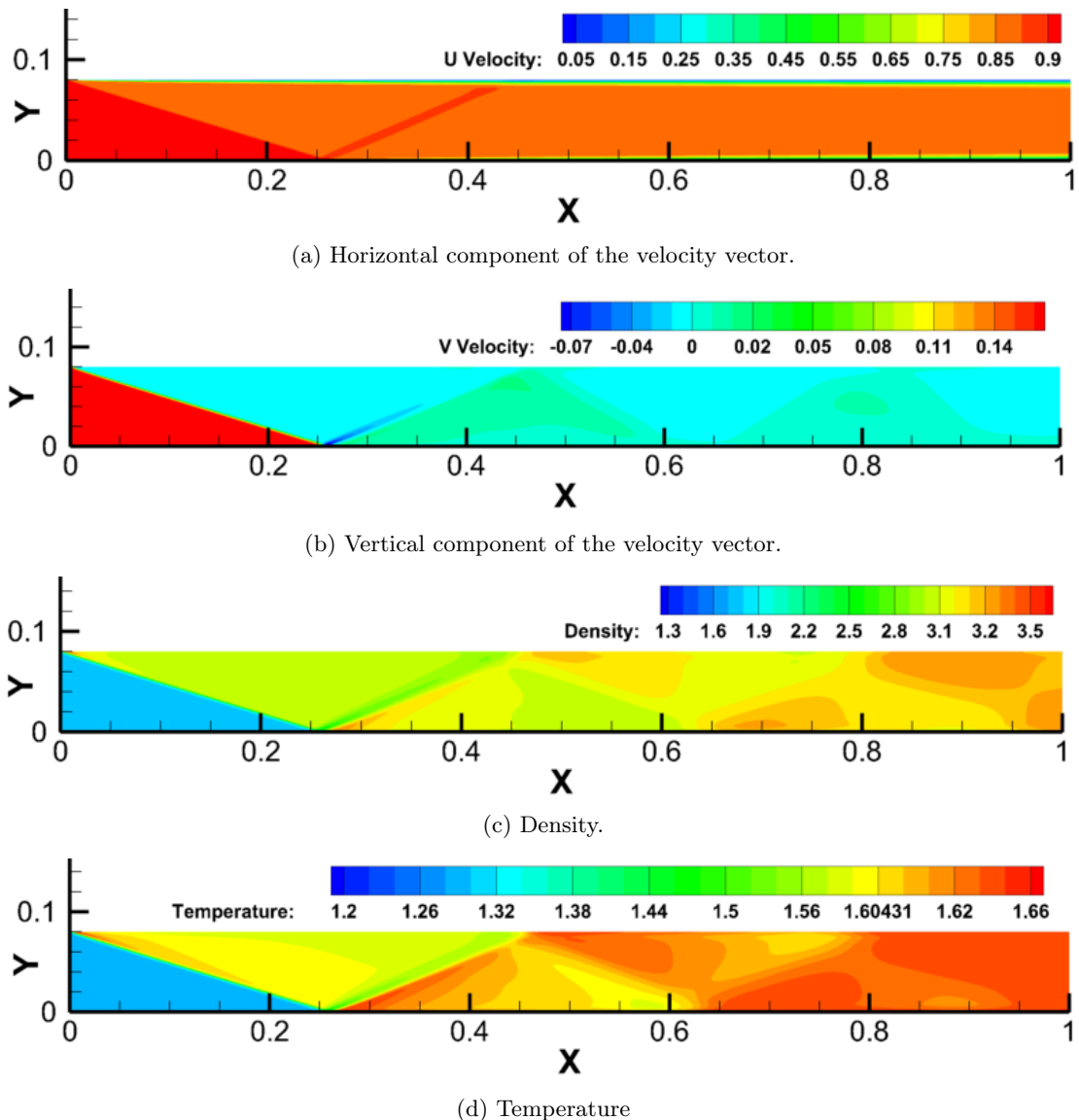


Figure 8: Primitive variables contour plot

Figures 8(a-d) provide information about the primitive variables. For 2D problems, these variables are ρ, u, v and T . Although these variables are derived from the conservation laws, they do not provide direct evidence of the flow field physics. (e.g. shocks, expansion waves, and vortical flow structures). However, an accurate prediction of the flow features is mandatory and must be done in an objective and consistent manner. Mendez *et al.* [22] provided an extensive survey of the shock wave detection methods and they demonstrated that specialized functions are required. In this study, we use the Flow Feature Extraction Functions (FFEF) shown in [22]. Figure 9 depicts the normal density gradient computed as:

$$\frac{d\rho}{dn} = \nabla\rho \cdot \frac{V}{|V|} \quad (12)$$

Unlike the gradient of the density, equation (12) computes the gradient of density in the direction of the velocity. Therefore, it only extracts region representing shocks and expansions waves whereas the gradient of density captures regions under large gradients, such as boundary layers. Figure 9 shows regions under positive

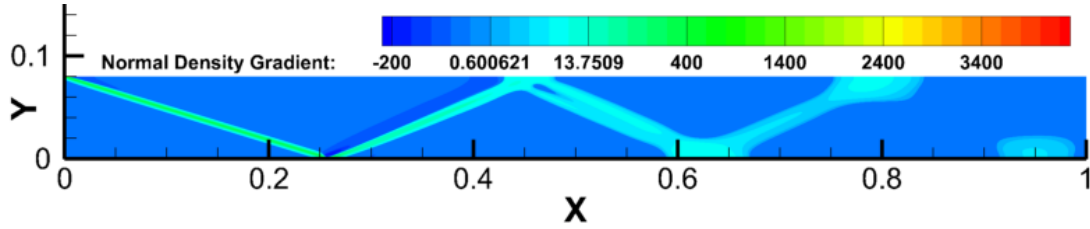


Figure 9: Normal density gradient.

values, representing compression waves, and a small region with negative values depicting expansion waves. The expansion waves are located near the leading edge tip in the bottom wall, where they are expected, as a result of the flow turning due to an oblique shock emanating from top leading edge tip, forcing the flow to go parallel to both walls. The shock structure found in this configuration is not symmetric, in contrast to [12] where they explored supersonic flow inside ducts. It is important to highlight the importance of the inflow. In duct analysis the inflow is assumed uniform throughout the inlet, in this study the inlet boundary conditions are based on the ramp angle shown in Figure 2 and thus a terminal normal shock at the outlet section is highly improbable, because of the oblique shocks.

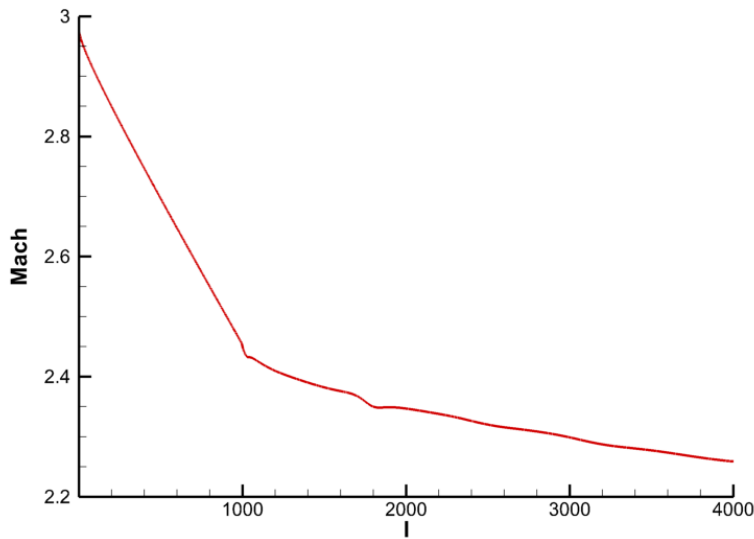
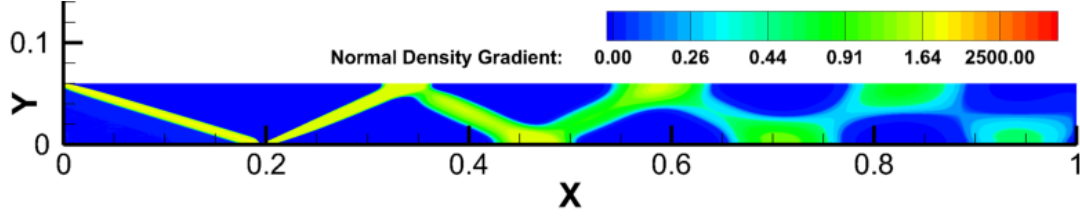


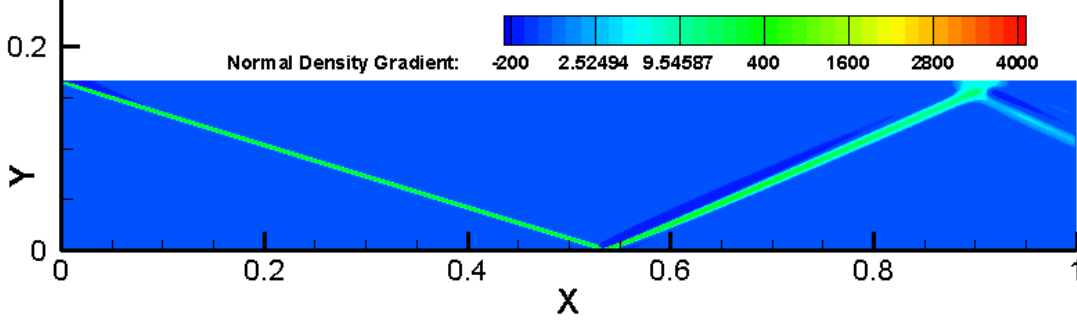
Figure 10: Averaged Mach Number.

Figure 10 shows the averaged Mach number in horizontal planes along the "X" axis. In Figure 10 the horizontal axis represents the computational coordinate " i ", from 1 to 4000, which is the maximum number of nodes in the horizontal direction. The compression process in the supersonic inlet is completed in three stages; flow decelerates from Mach 2.98 to a corresponding Mach number behind the strong oblique shockwave emanating from the tip of the ramp [Figure 2]. This effect is clearly shown by the steep slope in Figure 10 between $1 < i < 1000$. This deceleration is followed by weaker oblique shocks and represented by gradual changes in the Mach curve presented in Figure 10. The lowest averaged Mach number is around 2.3. Under these geometric parameters and flow conditions, the conditions at the outlet of the Isolator remain supersonic which is necessary for Scramjets.

Figure 11a and 11b represent the vertical component of the velocity vector for Case 1 and 3, respectively.



(a) Normal density gradient for Case 1



(b) Normal density gradient for Case 3

Figure 11: Shock structure

Figure 11 reveals important flow features and it demonstrates that the height of the Isolator influences the shock structure inside the Isolator. Figure 11(b) shows that only one reflected shock is present when the height is the maximum (Case 3), whereas the smallest height yields the maximum number of shock structures (Figure 11(a)). Figure 12 provides quantitative information about the efficiency of each geometric configuration. The static and total pressure averaged in vertical planes for the three different cases is shown in Figure 12. As anticipated, Case 1 will provide the highest static pressure recovery and highest total pressure loss. In contrast to Case 3, where the smallest static pressure recovery will be obtained, it leads to the lowest total pressure loss. Therefore we can conclude that Case 2 will provide the best option. However, the solutions show that none of the studied cases recovered the pseudo-shock length. By definition, the pseudo-shock length is the distance between the first "normal" shock to the end of the static pressure recovery region [12]. During the compression process the pseudo-shock is formed by the shock train, which is made up of the shock itself, and a mixing region that increases the static pressure without shock waves. Although Figure 12 represents the averaged value, it clearly shows that the bulk of pressure rise comes as a result of the strong oblique shock and the is followed by smaller pressures increments as a result of the weak reflect shocks. Those weak reflected shocks are represented by small "humps" in the static pressure lines. Nevertheless, the static pressure does not recover to the maximum expected value and this is demonstrated by the slope of the pressure lines which remain positive through the computational domain. These discrepancies are still under investigation however our initial conclusion is that this is because of the shock waves configuration. The shock correlations presented in [12] are valid for flow in ducts where normal shocks are present, which is not the case in this study, but they are under consideration future supersonic intakes studies.

3.3 Numerical Solution of the Flameholder Device, The Cavity

The previous section demonstrated that the flow remains supersonic in the cavity region of the Scramjet. This flow configuration has been studied in several experimental and computational works, interested readers should refer to [23–25]. Cavities play an important role in Scramjets by enhancing the mass exchange between the fluids, and the final goal is to increase the mixing efficiency to improve the combustion process while keeping low values of drag and acceptable total pressure losses. In addition, cavities are classified based on the length-to-depth ratio (L/D), where L is the length of the cavity and D is the depth. Cavities are considered open if $(L/D) < 10$, and closed if $(L/D) > 13$. This study considers a closed cavity, since $(L/D) = 60$. However, closed cavities have two important shortcomings, firstly, the drag is substantially high compared

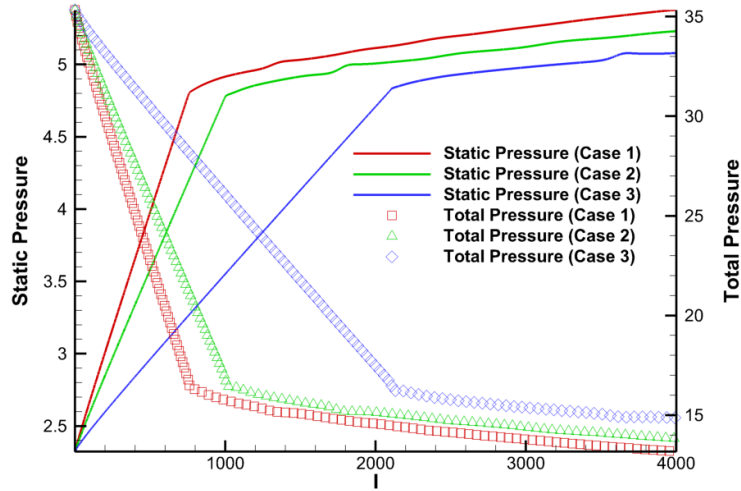


Figure 12: Averaged static and total pressure in Cases 1, 2 and 3

to open cavities and the fluid inside the cavity remains confined because of the cavity shear layer. [26] This provides an efficient means for flame stabilization, as a result of turbulent recirculation. However, this study represents the initial stage of a multiple projects, other cavity configurations will be considered in future studies.

Figure 13 illustrates the horizontal component of the velocity contour plot for the cavity flow when the inlet boundary conditions are supersonic. This flow configuration is named as *Clean flow* since the influence of the Isolator is not considered. As expected, the cavity shear layer is not formed rather the flow separates on the upstream leading edge of the cavity and reattaches in the cavity floor. To provide a better pictorial representation of the flow physics, the cavity region was divided into four sub-domains, please refer to Figure 6. The inlet, external flow region, outlet, and cavity section are called as Sub Domain II-a, Sub-Domain II-b, Sub-Domain II-c and Sub-Domain II-d, respectively.

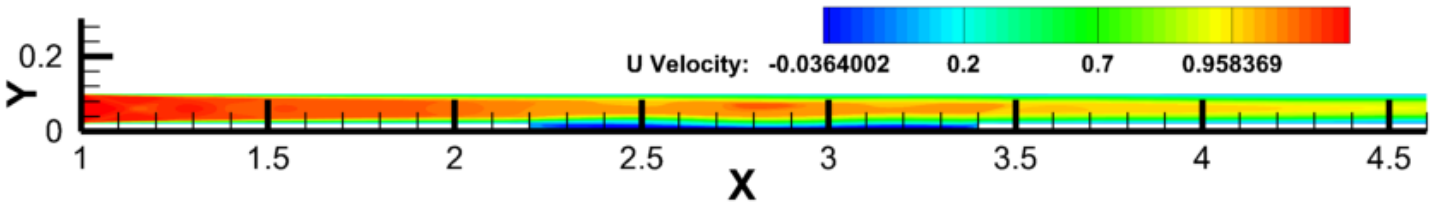


Figure 13: Horizontal component of the velocity vector contour plot

Figure 14 shows the horizontal component of the velocity vector for the Sub-Domains b, and d, representing the cavity region and the external flow section. Unlike open cavity flows where multiple recirculation zones appear, this picture shows two small areas where small vortices are present (bottom wall near the corners). In addition, the aspect ratio of this cavity causes the shear layer with a shape of "wave" yielding to a local acceleration region in the center of the cavity in the external flow section. As the flow approaches the cavity region, compression waves emanate from the leading edge corner, since the shear layer thickens near the leading edge corner. Therefore, the supersonic flow "sees" the thick shear layer as an obstacle. As the flow turns over the shear layer, expansion fans appear around $x = 2.5$ causing a local acceleration of the flow at $x = 2.7$. Again, the flow compresses in the near the aft corner causing compression waves around $x = 3.0$. To complement this explanation, the vertical component of the velocity vector and the pressure contour plot are shown in Figure 15 and Figure 16, respectively. Finally, this demonstrates the deficiency of closed cavities as a stable means for combustion processes since the wave-like shear layer causing a transient behavior producing unstable flames [23].

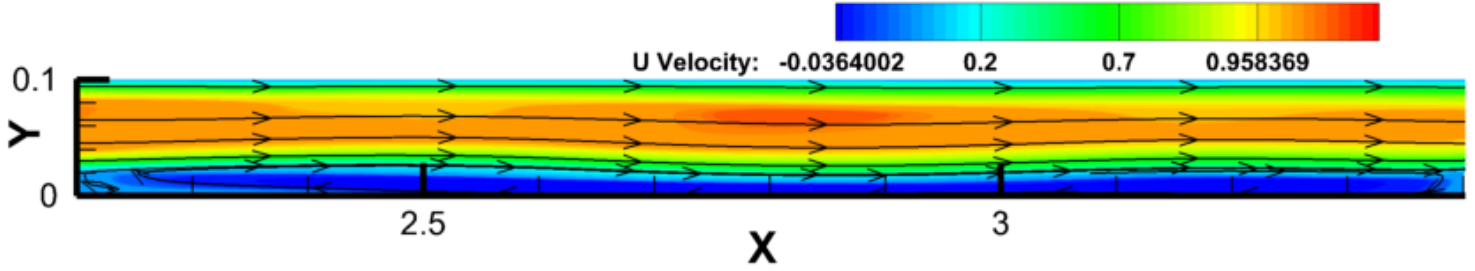


Figure 14: Horizontal component of the velocity vector contour plot in the cavity region

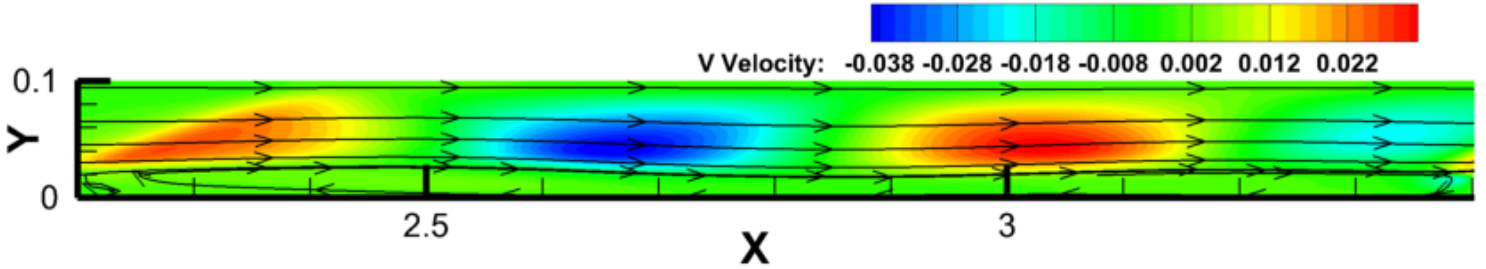


Figure 15: Vertical component of the velocity vector contour plot in the cavity region

Figure 17(a) illustrates the horizontal component of the velocity vector contour plot. As we demonstrated, the IDS was able to recover the physical solution expected under the conditions imposed in this study, which similar conditions have been addressed in experimental data and numerical studies, refer to [12]. Firstly, the boundary layer grows in the direction of the flow as expected and it thickens. As the flow goes through oblique shocks the flow decelerates locally, whereas in other regions the flow experiences local acceleration because of the "squeezing" effect from the thickening of the boundary layer. As it was expected, the flow field looks symmetric in the inlet section, which is common in this type of flow analysis when a uniform flow is prescribed. On the other hand, we can infer from Figure 17(b) that the interaction between shocks and boundary layer cause a little bulge on the boundary layer causing weak expansions fans and depicted by constant change on the sign of the vertical component of the velocity vector. Although the shock-boundary interaction does not cause local separation, this is evident in the first section of the duct. figures 17(c - d) demonstrates the flow experiences a compression process as it is expected in supersonic diffusers. Armed with this facts, we conclude that this numerical study represents an actual flow which is more complicated than idealized flows, one idealization of a similar flow configuration is adiabatic flow with friction in a constant area duct. However, this study represents a multi-dimensional frictional flow with an expansion-contraction region (cavity); and as such real flows are more complicated than the simple friction and therefore we cannot use simplified models to describe such fluid flows.

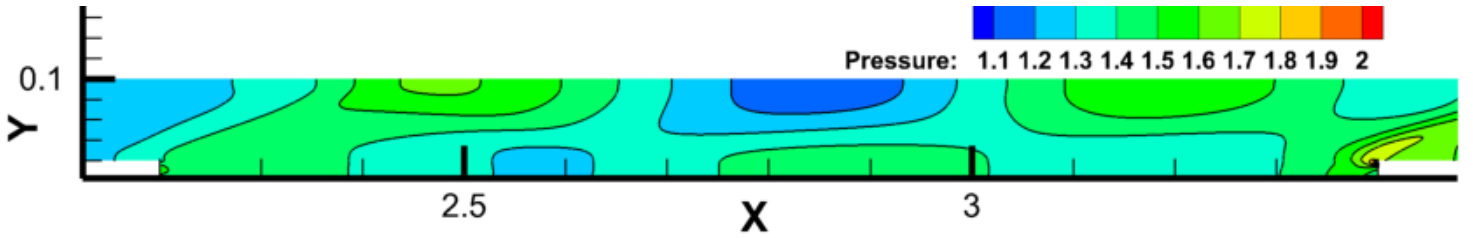
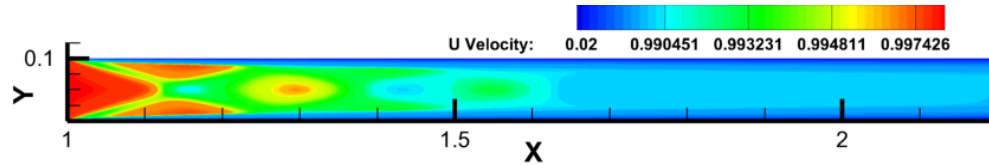
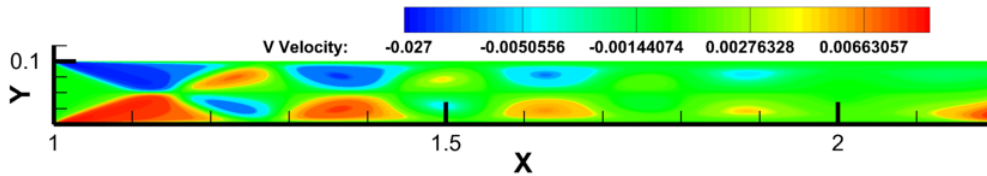


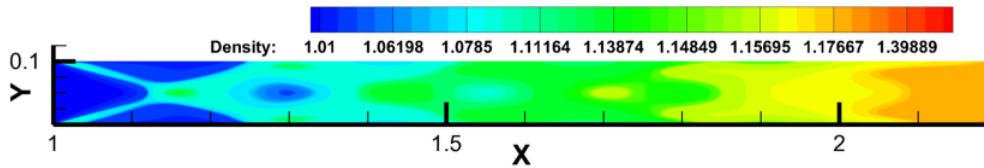
Figure 16: Pressure contour plot in the cavity region



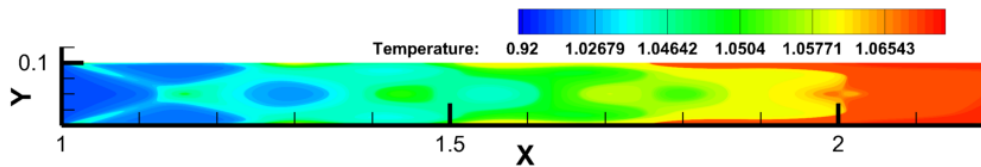
(a) Horizontal component of the velocity vector.



(b) Vertical component of the velocity vector.



(c) Density.



(d) Temperature

Figure 17: Primitive variables contour plot for the Sub-Domain II-a

The normal density gradient computed from equation (12) is depicted in Figure 18. It is widely accepted in the literature that for Mach numbers greater than 1.5, the shock structure expected in a duct is a shock train [27]. As shown, the IDS captured the shock train precisely based on the boundary conditions imposed in this study. Although the first half of the duct present strong shocks, and therefore the presence of such shocks can be inferred from the primitive variables, equation (12) demonstrated that the IDS was also capable of recovering the weak reflected shock. Examining closely Figure 18, we see that the oblique shock starts at the leading edge of the duct due to the no-slip boundary condition. The initial shock wave is reflected and because of the interaction with the boundary layer, weak expansions fans are also present and depicted by negative values. This interaction namely compression shock, expansion and boundary layer continues down the duct while gradually increasing the static pressure.

One striking conclusion from Figure 18 is that most of the approximate techniques to determine the

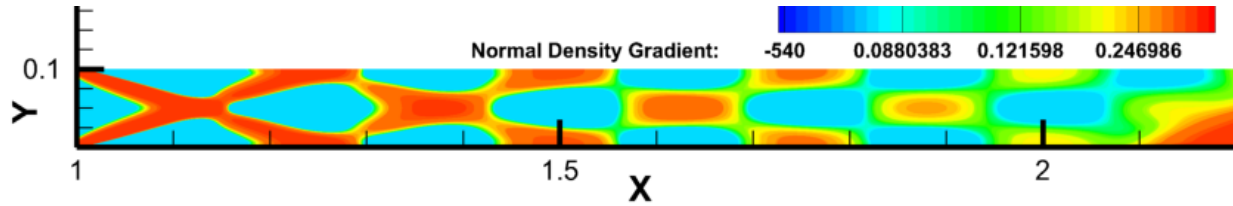


Figure 18: Normal density gradient for the Sub-Domain II-a

length of Isolator are based on supersonic diffusers (ducts) like the one shown in Figures 17-18. Although these approximate models are quite physically transparent the fluid dynamics involved in such devices is quite complex. Therefore, the designer must know the length of the Isolator upfront and predict the right length of the shock train is not a trivial task. For example, Sub-Domain II-a (Figures 17-18) is the right representation of a supersonic diffuser and therefore Figure 5 provides an accurate approximation of the length of the pseudo-shock for this case. The $L_p/D = 15$ for this case, and as a result, the length defined for this section should be long enough to efficiently recover the static pressure. This is clearly shown by the averaged static pressure line (green line) in Figure 19 where the pressure line reaches the plateau. However, the shock train shown in Figure 18 increases the pressure only by 26%, refer to Figure 19. Whereas the pressure recovery depicted in Figure 7 is around 130% and most of the recovery comes as a result of the strong shock wave emanating from the cowl, and a small portion from the Isolator itself, around 6.80%. In conclusion, air-breathing engine analysis requires the coupling of the full Scramjet for an appropriate design and analysis; and others parameters such as back pressure, confinement effect, Reynolds number and viscous effects must also be properly addressed to complement the estimations of L/D provided by such techniques.

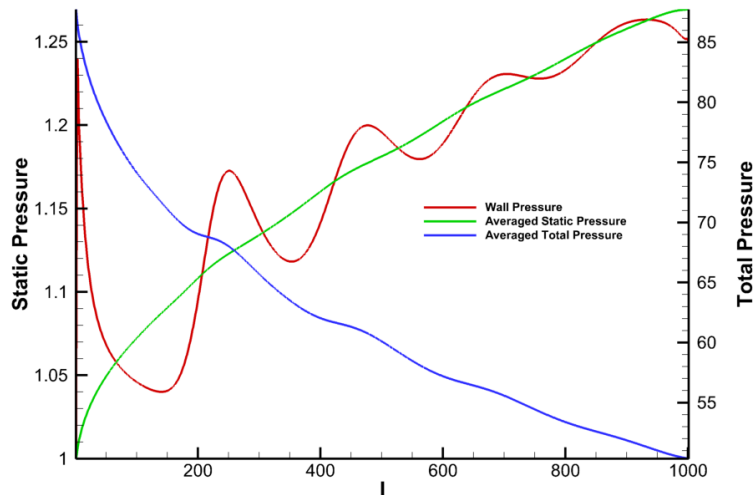


Figure 19: Pressure plots

3.4 Numerical Solution of the Full Domain

The previous subsection demonstrated the importance of coupling the cowl section, Isolator and the cavity region, which configuration in this study is referred to as the Full Domain or as the Scramjet. Although a uniform flow inlet boundary condition is widely used, this subsection pretends to set an objective study of such assumptions. As Figure 19 showed the static pressure recovered in the supersonic diffusion (Sub Domain II-a) was 26% whereas in the Full Domain configuration the pressure increased only by 16%. It is not surprising this solution since the Sub Domain II-a for the Full Domain configuration (Scramjet) acts as an extension of the Isolator resolved in Domain I, which results were presented in subsection 3.2 of this study. In addition to this, the velocity field in the region above the cavity presents considerable differences

compared to the "*Clean Flow*" configuration. Figure 20 depicts the horizontal component of the velocity vector and it clearly shows a large recirculation region on the top wall. Although the shear layer retains the same wave-like shape, recirculation zone yields to a non-symmetric shear layer. The causes of this asymmetry and this low momentum region on the top wall are still under study. However, Ben-Yakar *et al.* [28] studied the longitudinal cavity oscillation in closed cavities. They found that unsteady motions of the shear layer above the cavity are responsible for the instabilities that cause the shear layer to deflect upwards.

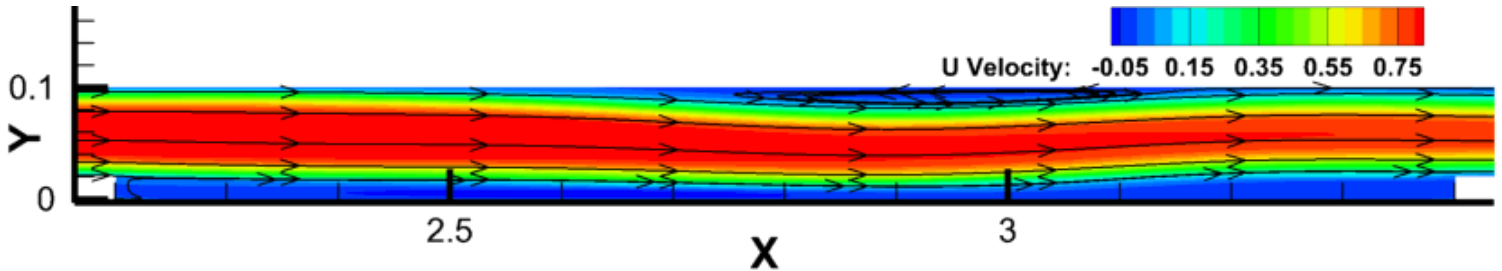


Figure 20: Horizontal component of the velocity vector contour plot in the cavity region

As it was expected, the averaged Mach number for each configuration differs greatly, refer to Figure 21. The Maximum averaged Mach number under the *Full Domain* configuration reaches values close to half of the *Clean Flow* configuration. This result is not surprising since the Full Domain considers the Isolator part from Domain I. Interesting to note that the averaged Mach number for the Full Domain configuration reaches its maximum value near the aft region of the cavity, what translates to expansions fans as it is expected in under these type of flow configurations. Furthermore, Figure 21 shows that both cavities experience a compression effect because of the oscillating shear layer, this is clearly depicted by the reduction of the averaged Mach number. Both flow configurations present this compression but the location at which the compression takes place is different, on average. This demonstrates the importance of considering the full Scramjet when flame holder devices are studied. Finally, is clearly noted in Figure 21 that the Full domain experiences a slight expansion in the last quarter of the cavity region. This expansion is the result of the separation of the boundary layer on the top wall, and finally, a weak recompression wave depicted in the averaged Mach number shown as a small increment in the Mach number. In conclusion, the combination of compression and expansion waves and the interaction with boundary layers differed greatly for these two type of flow configuration. Although the freestream conditions used in these two numerical studies were exactly the same, the role that the Isolator (Domain I) played influences the flow dynamics in the cavity region, and therefore in the shear layer. In addition to the Mach number, the acoustic waves present in this flow propagates in all direction at the local sound speed. Therefore, providing a suitable flame holder mechanism can vary greatly depending upon the type of flow configuration, for example the *Clean Flow* or *Full Domain*.

Figure 22a-c depicts the horizontal and vertical component of the velocity vector as well as the density contour plot for the Full Domain. Unlike Figures 8a-d, these figures present Domain I and the Sub Domain II-a. However, from Sub Domain II-a only half of the section is shown for sake of clarity. As it was expected the solution looks smooth in the junction between both computations. Remember that the inlet boundary conditions used in Sub Domain II were extracted from Domain I. Therefore, the first half section of Sub Domain II-a acts as an extension from Domain I. More specifically the section $0 \leq X \leq 1$ corresponds to the Isolator (Figure 2) and $1 \leq X \leq 1.5$ corresponds to the combustor part (Figure 1). This method proved to be efficient for supersonic flows when memory imposed technical limitations. The other interesting feature of this approach is that different mesh sizes can be used for each section, and the solution from one domain can be interpolated to the other domain using interpolating functions, such as Hermite splines. However, in this study, we used the same grid size. As it was depicted by Matsuo *et al.* [12] the shock train is followed by a "mixing region". This mixing region follows the shock train and it is clearly depicted in Figure 22-a. In this region there exist no shocks, but the pressure increases as in supersonic diffusers, refer to Figure 23.

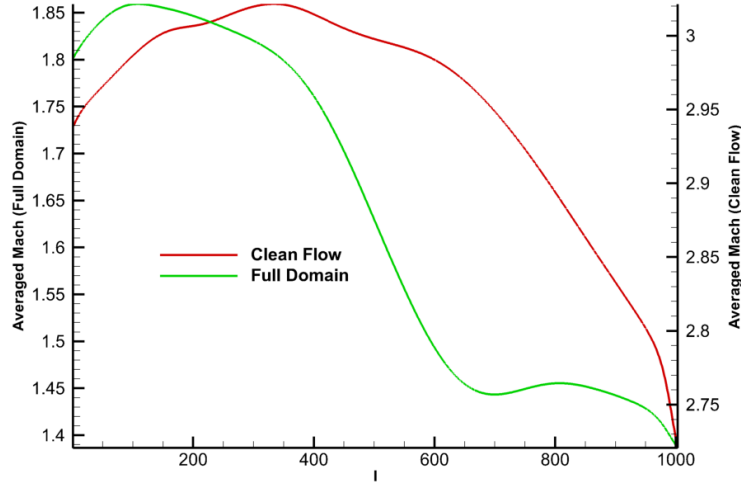


Figure 21: Mach number plots

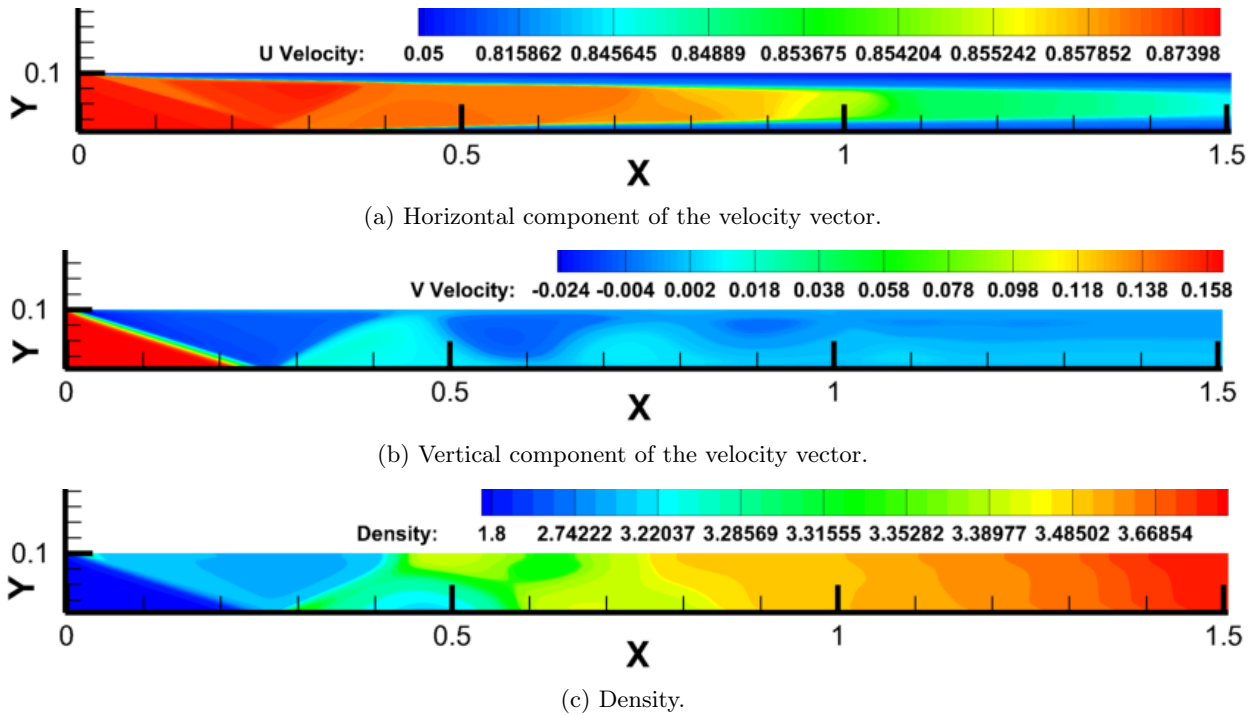


Figure 22: Primitive variables contour plot for the Full Domain

Figure 23 agreed with the physical expectations for this problem. As it was mentioned before the static pressure increases in the Sub-Domain to and it reaches a plateau and then decreases. The combination of Isolator and combustor part, allowed the pressure to reach its maximum value and decreases the Mach number to the values shown before. Therefore, we can conclude the IDS recovered the physics accurately. Also, the total pressure decreases drastically in the Isolator where strong shocks take place because of the cowl section, and then small reductions are found further down the Isolator. In conclusion, the IDS predicted the flow physics for all the different cases and demonstrated that approximate models for Isolator design underpredict the appropriate length for Isolators. As it was mentioned before, this is not a trivial task and most of the empirical correlations are built upon the assumption of inviscid flows and viscous phenomena

are rather important. More specifically, the actual L_p/D is 24.5 instead of 12 as it was explained in section 3.1, similar findings were presented by [27].

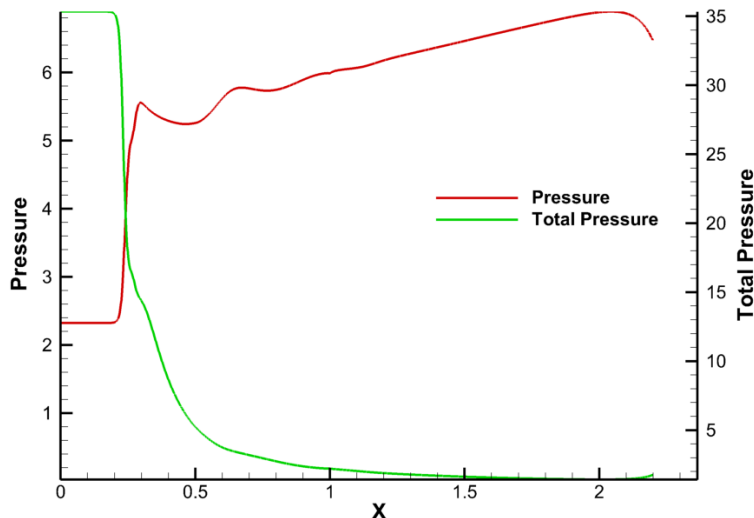


Figure 23: Pressure plots

4 Conclusion

The 'Integro-Differential Scheme' IDS is a relatively new approach to solve the integral form of the Navier-Stokes equations, based on two fundamental types of control volumes, spatial and temporal cells. Its past applications have demonstrated limited success and as a result, a high efficient parallel algorithm with MPI-OpenMP libraries was used. In addition to this, cloud Computing demonstrated being a great tool for computational scientists. This work focused on the Isolator Pseudo-Shock Train problem demonstrating that the IDS was able to predict the physics accurately and it showed very good agreement with the physical expectations and also we demonstrated that viscous phenomena should be considered for future development of empirical correlations. Finally, it is important to highlight that the authors pretend to extend this work to more complex scenarios such as flow injections and different L/D ratios. It is interesting to note that there is not a straightforward approach for Scramjet design and every effort to understand the complex physics inside this devices is worth taking. At this stage of the IDS development, it is yet to demonstrate how well it can predict the realistic 3-Dimensional fluid flow physics associated with turbulence. The problem of turbulence still remains the most vexing problem in fluid dynamics.

References

- [1] Gafar Abbas Elamin. *The Integral-differential Scheme (IDS): A New CFD Solver for the System of the Navier-Stokes Equations with Applications*. PhD thesis, North Carolina Agricultural and Technical State University, 2008.
- [2] Zun Cai, Zhenguo Wang, Mingbo Sun, and Xue-Song Bai. Effect of combustor geometry and fuel injection scheme on the combustion process in a supersonic flow. *Acta Astronautica*, 129:44 – 51, 2016.
- [3] Navin Kumar Mahto, Gautam Choubey, Lakka Suneetha, and K.M. Pandey. Effect of variation of length-to-depth ratio and mach number on the performance of a typical double cavity scramjet combustor. *Acta Astronautica*, 128:540 – 550, 2016.

- [4] Zun Cai, Xiao Liu, Cheng Gong, Mingbo Sun, Zhenguo Wang, and Xue-Song Bai. Large eddy simulation of the fuel transport and mixing process in a scramjet combustor with rearwall-expansion cavity. *Acta Astronautica*, 126:375 – 381, 2016. Space Flight Safety.
- [5] Zhenguo Wang, Zun Cai, Mingbo Sun, Hongbo Wang, and Yanxiang Zhang. Large eddy simulation of the flame stabilization process in a scramjet combustor with rearwall-expansion cavity. *International Journal of Hydrogen Energy*, 41(42):19278 – 19288, 2016.
- [6] Yiyu Han, Yuanyuan He, Ye Tian, Fuyu Zhong, and Jialing Le. Assessment of a hybrid rans/les simulation method and urans method in depicting the unsteady motions of flow structures in a scramjet combustor. *Aerospace Science and Technology*, 72:114 – 122, 2018.
- [7] M. Berglund and C. Fureby. Les of supersonic combustion in a scramjet engine model. *Proceedings of the Combustion Institute*, 31(2):2497 – 2504, 2007.
- [8] C. Fureby, M. Chapuis, E. Fedina, and S. Karl. Cfd analysis of the hyshot ii scramjet combustor. *Proceedings of the Combustion Institute*, 33(2):2399 – 2405, 2011.
- [9] Johan Larsson, Stuart Laurence, Ivan Bermejo-Moreno, Julien Bodart, Sebastian Karl, and Ronan Vicquelin. Incipient thermal choking and stable shock-train formation in the heat-release region of a scramjet combustor. part ii: Large eddy simulations. *Combustion and Flame*, 162(4):907 – 920, 2015.
- [10] K. Nordin-Bates, C. Fureby, S. Karl, and K. Hannemann. Understanding scramjet combustion using les of the hyshot ii combustor. *Proceedings of the Combustion Institute*, 36(2):2893 – 2900, 2017.
- [11] Frederick Ferguson, Nastassja Dasque, Mookesh Dhanasar, and Leonard Uitenham. An aerodynamic analysis of the generic hypersonic vehicle. In *2018 AIAA Aerospace Sciences Meeting*, page 0637, 2018.
- [12] Kazuyasu Matsuo, Yoshiaki Miyazato, and Heuy-Dong Kim. Shock train and pseudo-shock phenomena in internal gas flows. *Progress in Aerospace Sciences*, 35(1):33 – 100, 1999.
- [13] John David Anderson. *Modern compressible flow: with historical perspective*, volume 12. McGraw-Hill New York, 1990.
- [14] Frederick Ferguson, Julio Mendez, and David Dodoo-Amoo. Evaluating the hypersonic leading-edge phenomena at high reynolds and mach numbers. In Serdar Celebi, editor, *Recent Trends in Computational Science and Engineering*, chapter 4. InTech, Rijeka, 2018.
- [15] Frederick Ferguson, Julio Mendez, David Dodoo-Amoo, and Mookesh Dhanasar. The performance evaluation of an improved finite volume method that solves the fluid dynamic equations. In *2018 AIAA Aerospace Sciences Meeting*, page 0834, 2018.
- [16] A Arovitola and FM Denaro. Using symbolic computation software packages in production of multidimensional finite volume-based large eddy simulation codes. *International Journal for Numerical Methods in Fluids*, 71(5):562–583, 2013.
- [17] S Seckin and KB Yuceil. Flow visualization of a scramjet inlet–isolator model in supersonic flow. In *EPJ Web of Conferences*, volume 45, page 01099. EDP Sciences, 2013.
- [18] Cheng-Peng Wang, Kun-Yuan Zhang, and Jin-jun Yang. Analysis of flows in scramjet isolator combined with hypersonic inlet. In *43rd AIAA Aerospace Sciences Meeting and Exhibit*, page 24, 2005.
- [19] Wei Huang, Zhen-guo Wang, Mohamed Pourkashanian, Lin Ma, Derek B Ingham, Shi-bin Luo, Jing Lei, and Jun Liu. Numerical investigation on the shock wave transition in a three-dimensional scramjet isolator. *Acta Astronautica*, 68(11-12):1669–1675, 2011.
- [20] Birgit U Reinartz, Carsten D Herrmann, Josef Ballmann, and Wolfgang W Koschel. Aerodynamic performance analysis of a hypersonic inlet isolator using computation and experiment. *Journal of Propulsion and Power*, 19(5):868–875, 2003.
- [21] Patrick J Roache. *Verification and validation in computational science and engineering*, volume 895. Hermosa Albuquerque, NM, 1998.
- [22] Julio Mendez, David Dodoo-Amoo, Mookesh Dhanasar, and Frederick Ferguson. Physics based validation of an improved numerical technique for solving thermal fluid related problems. 2017.
- [23] MR Gruber, RA Baurle, T Mathur, and K-Y Hsu. Fundamental studies of cavity-based flameholder concepts for supersonic combustors. *Journal of Propulsion and power*, 17(1):146–153, 2001.
- [24] Steven Beresh, Justin Wagner, and Brian Pruett. Particle image velocimetry of a three-dimensional supersonic cavity flow. In *50th AIAA Aerospace Sciences Meeting including the New Horizons Forum and Aerospace Exposition*, page 30, 2012.
- [25] Donald P Rizzetta. Numerical simulation of supersonic flow over a three-dimensional cavity. *AIAA journal*, 26(7):799–807, 1988.

- [26] Hongbo Wang, Zhenguo Wang, Mingbo Sun, and Ning Qin. Large eddy simulation based studies of jet cavity interactions in a supersonic flow. *Acta Astronautica*, 93:182 – 192, 2014.
- [27] William H Heiser and David T Pratt. *Hypersonic airbreathing propulsion*. AIAA, 1994.
- [28] Adela Ben-Yakar and Ronald K Hanson. Cavity flame-holders for ignition and flame stabilization in scramjets: an overview. *Journal of propulsion and power*, 17(4):869–877, 2001.